mathematics

Article

Predicting the Future Appearances of Lost Children for Information Forensics with Adaptive Discriminator-Based FLM GAN

Brijit Bhattacharjee [1], Bikash Debnath [2], Jadav Chandra Das [3], Subhashis Kar [1], Nandan Banerjee [4], Saurav Mallik [5,6,*] and Debashis De [7]

1 Department of Computer Science and Engineering, Swami Vivekananda Institute of Science & Technology, Kolkata 700145, West Bengal, India
2 Amity Institute of Information Technology, Amity University, Kolkata 700135, West Bengal, India
3 Department of Information Technology, Maulana Abul Kalam Azad University of Technology, West Bengal, Haringhata 741249, West Bengal, India
4 Department of Computer Science and Engineering, Sikkim Manipal Institute of Technology, Majitar 737136, Sikkim, India
5 Department of Environmental Health, Harvard T. H. Chan School of Public Health, Boston, MA 02115, USA
6 Department of Pharmacology & Toxicology, The University of Arizona, Tucson, AZ 85721, USA
7 Department of Computer Science and Engineering, Maulana Abul Kalam Azad University of Technology, West Bengal, Haringhata 741249, West Bengal, India
* Correspondence: sauravmtech2@gmail.com or smallik@arizona.edu

Abstract: This article proposes an adaptive discriminator-based GAN (generative adversarial network) model architecture with different scaling and augmentation policies to investigate and identify the cases of lost children even after several years (as human facial morphology changes after specific years). Uniform probability distribution with combined random and auto augmentation techniques to generate the future appearance of lost children's faces are analyzed. X-flip and rotation are applied periodically during the pixel blitting to improve pixel-level accuracy. With an anisotropic scaling, the images were generated by the generator. Bilinear interpolation was carried out during up-sampling by setting the padding reflection during geometric transformation. The four nearest data points used to estimate such interpolation at a new point during Bilinear interpolation. The color transformation applied with the Luma flip on the rotation matrices spread log-normally for saturation. The luma-flip components use brightness and color information of each pixel as chrominance. The various scaling and modifications, combined with the StyleGan ADA architecture, were implemented using NVIDIA V100 GPU. The FLM method yields a BRISQUE score of between 10 and 30. The article uses MSE, RMSE, PSNR, and SSMIM parameters to compare with the state-of-the-art models. Using the Universal Quality Index (UQI), FLM model-generated output maintains a high quality. The proposed model obtains ERGAS (12 k–23 k), SCC (0.001–0.005), RASE (1 k–4 k), SAM (0.2–0.5), and VIFP (0.02–0.09) overall scores.

Keywords: StyleGan ADA; GAN; deep learning; lost children

MSC: 68T07

check for updates

Citation: Bhattacharjee, B.; Debnath, B.; Das, J.C.; Kar, S.; Banerjee, N.; Mallik, S.; De, D. Predicting the Future Appearances of Lost Children for Information Forensics with Adaptive Discriminator-Based FLM GAN. *Mathematics* **2023**, *11*, 1345. https://doi.org/10.3390/math11061345

Academic Editor: Ivan Lorencin

Received: 23 January 2023
Revised: 1 March 2023
Accepted: 6 March 2023
Published: 10 March 2023

1. Introduction

This article aims to show a deep learning-based investigation method for missing children's cases. A breach of the law in disappearing children cases increases the risks of exploitation through criminal activity. A detailed description of the lost children, recorded through the initial investigation, leads to failure as after a few years, the missing children's faces start to change with aging. Our method tries to predict the aging effect while presenting the personalized attributes of the children's faces. The supervised-based DNN explored in this literature requires a range of faces of a similar object for a long time to perform training. In recent years, GAN and its variant (viz., cGAN) achieved poor performance compared to physical and prototype-based methods [1–3] to train the facial aging method with solitary data. The Tufts [4] face dataset are used to evaluate the performance of the proposed work. cGans-based [5–8] approaches fail to achieve the demands for picture quality (i.e., aging precision and identity retention) while training the network to understand the effects of aging between the two rare age groups.

On the contrary, GAN tries to increase the performance by loading facial attribute vectors into the generator and discriminator by presenting the congruent face characteristics. Therefore, these works offer a StyleGan ADA [1] based framework to generate the prediction. The StyleGan ADA feed discriminator with information about the type of errors produced by generator. The statistical evaluation of activation function performs real and model generated data identification through feature matching. The proposed approach was tested with multiple hyperparameters using the KinFaceW dataset. The best accuracy was achieved with F1L2M8 hyperparameter, where F1 represents the feature map as $1\times$, L2 is the learning rate set to 2 and M8 as 8 parameter mapping net depth. F1L2M8 obtains a 10–30 BRISQUE score for the image quality using KinFaceW-I and KinFaceW-II datasets. The model-generated outputs obtain MSE (2 k–5 k), RMSE (4–7), PSNR (10–14), SSIM (0.2–0.5), UQI (0.7–0.8), and MSSSIM (0.2–0.5).

2. Related Works

A latent distribution strategy using generator mapping was implemented by Fokker Plank [9] in the data space. It includes a plug-and-play facility to use directly the pre-trained GAN [10] models. The article consists of several rigorous experiments on the complex data distribution. It has Wasserstein gradient flow with the convexity of the f-divergence method [11] that preserves informational identity by evaluating applicability for structural correspondence. The following approach utilizes the FRGS-V2 dataset to generate real-life application scenarios. We compare the results with the MAD and SOTA procedures. To maintain robust and accurate performance, MIPGAN [11] applies Arcface. MIPGAN [11] Combined few pre-trained GAN architectures to produce images maintaining perceptual quality metrics. MIPGAN minimizes binary cross entropy loss by balancing inner product between real and generated samples. This GAN framework avoid generation of unrealistic samples from distance-based objectives. The generated data are re-digitized for morphing attack detection mechanisms. Applying deformation via prints or lines controls the image curves in MLS [12]. In [12], it implements the slightest square deformation to produce a linear system from partial derivatives of the plotted matrix. MLS represents affine deformation for stretching the result. Uniform scaling is updated with similarity deformation to learn from observations. Rigid deformation iterates eigenvalue and vectors for covariance evaluation. In Automatic Interpolation and Recognition (AIRF) [13], new views are generated via linearly interpolated fields of the given input. This evaluation mechanism uses Gaussian probability distribution for approximation. AFR [14] applies discrete cosine transformation to classify featured vectors. It combines Benford features with the linear support vector machine as the classifier. [15] proposed a distribution scale-specific latent factor variation to quantify disentanglement.

3. Major Contribution

- The proposed approach generates future faces that help to continue the investigation, using the Tufts [4] dataset.
- The BRISQUE quality metrics are analyzed to illustrate model-generated images' visual quality using KINFACE I and KINFACE II datasets.
- An extensive experiment was carried out to compare the original parent image with the model-generated children's ideas of equal age using MSE, MSSSIM, ERGAS, SCC, RASE, SAM, and VIFP.

- Various hyper parameters such as F1L2M8, F2L3M5, F2L2M8, F1L3M7, and F2L4M3 compare the proposed model-generated images.

4. Background Analysis

We use the convolution method as a kernel to extract features from images and modify the input as a matrix, referred to as a kernel which enhances the output. During this modification process, V as a convolution kernel with probability h, normally distributed, is measured as $Z_\theta(e) = V \times e + \theta$ [1]. Instead of manual extraction by Equation (1), CNN learn v extracts latent feature e by $Z_\theta(e)$. The following are a few important properties of the Cauchy distribution:

- Multidimensional Cauchy distribution can be used to fill the latent space for any random variable u:

$$\mathrm{C}\nu(\mathrm{u}) = \frac{\frac{1}{\pi}}{1+\mathrm{u}^2} \forall\ \mathrm{u} \in \mathbb{R} \quad (1)$$

Here, $\frac{1}{\pi}$ act as a density function.

- In the absence of an appropriate moment generating function, the characteristic function is defined as follows:

$$\Phi_{\mathrm{u}}(\nu) = \mathrm{E}\left[\mathrm{e}^{\mathrm{i}\nu\mathrm{U}}\right] \quad (2)$$

where $\mathrm{i} = \sqrt{-1}$ and v is a real number

$$\left|\Phi_{\mathrm{u}}(\nu)\right| = \left|\mathrm{E}\left[\mathrm{e}^{\mathrm{i}\nu\mathrm{U}}\right]\right| \leq \mathrm{E}\left[\left|\mathrm{e}^{\mathrm{i}\nu\mathrm{U}}\right|\right] \leq 1$$

$\left|e^{ivU}\right| = 1$, where v is a real valued random variable.

- The value of distribution $\Phi_u(\nu)$ greater than one may produce a negative impact on the GAN training process. It leads to the inappropriate formation of data points for generator-generated samples.
- In order to train the proposed GAN model with latent space e, n independent random variables $U_1, U_2, \ldots, U_N$ are distributed with a fixed latent probability distribution as follows:

$$U_1 + U_2 + \ldots + U_N(\nu) = \Phi\ \mathrm{U1}(\nu)\Phi\ \mathrm{U2}(\nu)\Phi\ \mathrm{U3}(\nu)\ \ldots.\Phi\ \mathrm{Un}(\nu) \quad (3)$$

- The augmentation strategies in our proposed work are closely related to the approaches referred to as random masking [16]. This combines regularizing with augmentation of the existing data for better model performance: the projection of a random subset of dimension interpreted by cut-out augmentation. For a set of deterministic projections $R_1, R_2, \ldots, R_{N,}$ the condition is defined as $R_i^2 = R_i$. Such projections include pixel permutation [17], scaling, and squeezing [18–20]. The discrete probabilities to choose identity operator O_i are $r_{0,}r_1, \ldots\ r_{\mathrm{n}}$. For remaining discrete probabilities, it is $\mathrm{R_K}$. The mixed form of the projection is represented as follows:

$$\mu_\rho = r_0 O_i + \sum_{i=1}^{N} r_i R_i \quad (4)$$

For probability distribution $\mathrm{z} \neq 0$ and $\mu_\rho \mathrm{z} = 0$, the representation of this combination becomes the following:

$$r_0 z + \sum_{i=1}^{N} r_i R_i z = \mu_\rho z = 0 = \sum_{i=1}^{N} r_i R_i z \ = -r_o z \quad (5)$$

Applying the theorem mentioned in Ambient GAN [21], probability for block pixel measurement, where n $\in t^{i} \in \mathbb{R}^{i}$ if $t > 1$, there exists a unique distribution ${t_n}^r$ and ${t_m}^g$ for a given dataset, $= \Omega\left(\frac{|t|^{2i}}{(1-t)^{2i}_{\epsilon^2}} \log\left(\frac{|t|^{i}}{\delta}\right)\right)$ where $\epsilon > 0$ and $\delta \in (0,1)$ Equation (5) becomes, $\sum_{i=1}^{N} r_i(z, R_i Z) = -r_0\langle Z, z\rangle$.

5. Proposed Method

Overview of the FLM approach represented in Figure 1. The proposed method performs pixel blitting by duplicating pre-existing pixels. This operation does not blend with adjacent pixels. The adjustments aggregate into a 3×3 matrix V with input pixel (a_i, b) placed as the output $[a_0, b, 1]^T = V \cdot [a_i, b_i, 1]^T x -$ flip applied to each transformation with probability P by sampling $i \sim \mu\{0,1\}$ uniform distribution, then update V by scale $(1-2i, 1) \cdot V$. If rotation is applied to sample $i \sim \mu\{0,3\}$, then V is updated to rotate $\left(-\frac{\pi}{2} \cdot i\right) \cdot V$. Apply the integer translation to sample $t_a, t_b \sim \mu(-0.125\,, +0.125)$. During this translation, V is updated to translate $(\mathrm{round}(t_a w), \mathrm{round}(t_b h)) \cdot$ Matrix V sample parameter s from a log normal distribution as $s \sim N\left(0, (0\,2, 1n^2)^2\right)$. Further general geometric transformation can be achieved by isotropic scaling of the sample $\theta' \sim \mu(-\pi, +\pi)$ and setting $\mathrm{Rotate}(-\theta) \cdot V$, then performing arbitrary rotation. Anisotropic scaling is performed along with fractional transformation with probability P by sample $t_a, t_b \sim N\left(0, (0.125)^2\right)$ and updating translate $(t_a w, t_b h) \cdot V$. Padding the image with reflection is done to avoid the unwanted effect of the image boundaries. The orthogonal low pass filter $O(z)$ calculates the amount of padding by (P_0, P_{ni}) = $\mathrm{CalcPad}(V, W, h, O(P))J = \mathrm{Pad}(J, P_{lo}, P_{hi}, \mathrm{reflect})$. Placing the origin at the image center is achieved by C = $\mathrm{Translate}\left(\frac{1}{2}w - \frac{1}{2} + P_{lo}\,, a\,,\ \frac{1}{2}h\,,\ P_{lo}\,,\ b\right)$ and $V = C \cdot V \cdot C^{-1}$. The method then upsamples J^{-1} =$\mathrm{Upsample}\left(J, \theta\left(z^{-1}\right)\right)$. Bilinear interpolation is applied to this higher resolution image. Down-sampling operation is applied to $(J, O(z))$. Finally, color transformation is applied to gather the parameters of each separate transformation into 4×4 matrix. Sample $\theta' \sim \mu(-\pi, +\pi)$ and setting $Rotate(-\theta) \cdot V$ is conducted, followed by then performing arbitrary rotation. Anisotropic scaling is performed with fractional transformation with probability P by sample $t_a, t_b \sim N\left(0, (0.125)^2\right)$ and updating translation $(t_a w, t_b h) \cdot V$.

5.1. Data Augmentation

Machine learning systems of image augmentation improve instance segmentation-based image policies. Applying augmentation policies in models during training improves performances and accuracy for learned data. The augmentation approaches improve model accuracy and robustness by reducing overfitting. Few approaches like jittering helps to generalize different lighting conditions of contrast and saturation. Concerning the neural architecture search (NAS), the selection of an improper optimization procedure leads to increased computational complexity and computation cost. The optimal magnitude influences the training procedure in population-based augmentation (PBA 1). In our proposed method, Rand Augment [11] reduces computational expense caused by the search phase implementing several search policies [1,10,22]. The proposed system uses uniform probability to choose transformation to maintain image diversity.

5.2. Pixel Blitting

In order to detect pixel level errors, the discriminator implements rotation for geometric transformation. The given image accumulates into a matrix M of pixel values. The probability P is applied with x flip upon matrix M by $M^{|} = x(M)$. The $M^{|}$ is then periodically updated by sampling via discrete $\mathcal{U}\{.\}$ or continuous $\mathcal{U}(.)$ uniform distribution. 90°

rotation is applied with sample $\rangle \sim \mathcal{U}\{0,3\}$. Finally, the $M_R^{|}$ updated $\left(M^{|} \leftarrow M_R^{|}\right)$ to $T\left(M_R^{|}\right)$ by applying the translation matrix.

$$T = \begin{bmatrix} 1 & 0 & 0 \\ 0 & 1 & 0 \\ -0.125 & 0.125 & 1 \end{bmatrix} \tag{6}$$

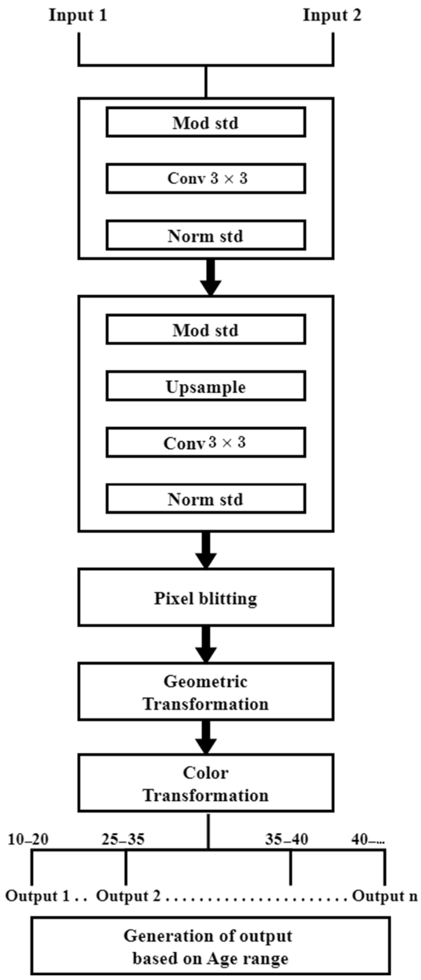

Figure 1. Overview of the proposed FLM method.

5.3. Geometric Transformation

The proposed approach starts sampling t normally distributed with mean 0 and variance 1. The parameter S is evaluated via base 2 exponent of 0.2∗ t. Sample S is log normally distributed with $\mu = 0$, $\sigma^2 = (0.2 \cdot \ln \cdot 2)^2$. The previous probability is updated to $P^{|} \leftarrow 1 - \sqrt{1 - P}$. The proposed approach performs uniform distribution upon sample θ with parameter $-\pi$ and π. The previous pixel matrix is again updated as follows:

$$T^{|}\left(M_R^{|}\right) \leftarrow \begin{bmatrix} -\cos\theta & \sin\theta & 0 \\ -\sin\theta & -\cos\theta & 0 \\ 0 & 0 & -1 \end{bmatrix} T\left(M_R^{|}\right) \tag{7}$$

After anisotropic scaling again with probability P, the parameters of the translation matrix show a normal distribution with mean 0 and variance $(0.125)^2\left[T^{||}\left(M_R^{|}\right)\right]$. The geometric transformation is executed by setting up padding based on reflection. The amount of padding is evaluated based on $T''(M'R)$ bilinear interpolation that is carried out through up-sampling and down-sampling of isotropic scaling value interpolation. The proposed approach uses sym6 to maintain the balance between model execution cost and sampling quality.

5.4. Color Transformation

The transformation starts by setting a homogeneous $3d$ transformation brightness which is applied based on the probability where samples are normally distributed with $\mu = 0$ and $\sigma = 0.2$. Uniform distribution is applied to achieve a Luma flip. We carried out Hue notation via a rotation matrix and ended the process with saturation through log-normal distribution.

6. Results

6.1. The proposed model accuracy evaluation with Similarity Index Evaluation Metrices

Image Quality Assessment (IQA) compares the amount of degradation with the perceived image. Inappropriate correlation leads to a reduction of image quality and was reflected as noise. Transmission, compression, enhancement, and acquisition are the features that play an essential role in the case of visual information analysis. Tables 1 and 2 were performed on naturally existing persons. The model generated column contains images generated via the FLM approach compared with the original image. We chose children aged between 7 and 18 years for this experiment with their birth parents. The Image Quality Assessment quantifies with the mean square error (MSE) [21]. It evaluates the quality via the mean square deviation method.

$$\mathrm{MSE} = \frac{1}{\mathrm{IJ}} \sum_{j=0}^{I} \sum_{i=1}^{J} \left[\hat{k}(x,y) - k(x,y)\right]^2 \tag{8}$$

Table 1. MSE, RMSE, PSNR, and SSIM evaluation on real existing persons using the proposed approach.

Model Generated Image	Original Image	MSE	RMSE	PSNR	SSIM
		3505.1024	40.0425	12.5616	(0.3667, 0.5163)
	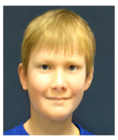	3605.1084	30.0425	11.4312	(0.4334, 0.5132)
	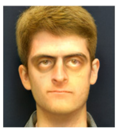	1505.1034	48.0316	13.2114	(0.4667, 0.4328)
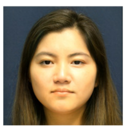	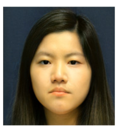	1202.6273	41.8561	11.1255	(0.4107, 0.4630)
	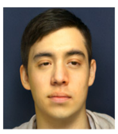	1403.6883	42.5757	13.2367	(0.5817, 0.5532)

Table 1. *Cont.*

Model Generated Image	Original Image	MSE	RMSE	PSNR	SSIM
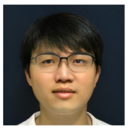	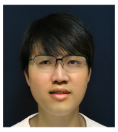	1515.6861	41.5731	14.1244	(0.3836, 0.4111)
		6419.2100	80.1199	10.0559	(0.2712, 0.3246)
		1906.7972	43.6668	15.3277	(0.4908, 0.5103)

Here, MSE evaluation is conducted between two images, $K(m,n)$ and $\hat{K}(m,n)$, to obtain the forecasting error root mean square error used to evaluate the absolute error.

$$\text{RMSE } = \sqrt{MSE} \tag{9}$$

PSNR (Peak Signal to Noise Ratio) [21] uses the logarithmic decibel scale to obtain a wide dynamic range. A ratio is obtained of possible signal power compared with distorting noise. The evaluation is expressed as follows:

$$\text{PSNR } = 10\log_{10}\left(\mathrm{p}^2\right)/\mathrm{MSE} \tag{10}$$

where p represents the peak value. Important perception-based facts are evaluated with the help of the Structure Similarity Index (SSIM) [21]. The measurement is expressed as follows:

$$\text{SSIM } = \rceil_N(m,n).\prod_{K=1}^{N} F_K(m,n)T_K(m,n\ ) \tag{11}$$

where the scale N represents the highest scale, $F_K(m,n)$ represents the contrast compression, and $T_K(m,n)$ represents the structure compression. $\rceil_N(m,n)$ is the compression based on luminance. They are evaluated by the following equations:

$$\rceil_N(\mathrm{m},\mathrm{n}) = \frac{2\mu_m\mu_n + c_1}{\mu_m^2 + \mu_n^2 + c_1} \tag{12}$$

$$F_K(\mathrm{m},\mathrm{n}) = \frac{2\sigma_m\sigma_n + c_2}{\sigma_m^2 + \sigma_n^2 + c_2} \tag{13}$$

$$T_K(\mathrm{m},\mathrm{n}) = \frac{\sigma_{mn} + c_3}{\sigma_m\sigma_n + c_3} \tag{14}$$

Here, μ_m, μ_n are the local mean, $\sigma_m, \sigma_n =$ standard deviation and σ_{mn}= covariance for image.

The evaluation based on Tables 1 and 2 observes that the MSE score ranges from 1 k to 5 k. Results with MSE score below 6 k expected to be perfect for similarity index. The proposed approach obtains RMSE between 30 and 80; lower RMSE reflects better accuracy. The PSNR score in Table 1 is better in comparison to Table 2. SSIM index also scores better for the proposed method.

Table 2. MSE, RMSE, PSNR, and SSIM evaluation on sample images.

Model Generated Image	Original Image	MSE	RMSE	PSNR	SSIM
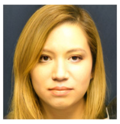	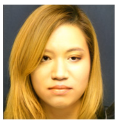	2235.0545	50.3423	12.8512	(0.5127, 0.5687)
		2347.4649	45.3470	14.2722	(0.5032, 0.6289)
		2213.8913	41.0704	12.6132	(0.5381, 0.6013)
		2532.1281	46.3587	11.5791	(0.6212, 0.6864)
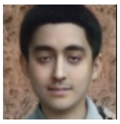		2730.0744	52.2501	13.7690	(0.5308, 0.6178)
		2402.9915	49.0203	14.3232	(0.5122, 0.5651)
		2156.5758	46.4389	14.7931	(0.5032, 0.6289)
		5314.2476	72.8988	10.8763	(0.5459, 0.5977)

6.2. FLM Model Performance Evaluation-Based Multiscale Extension, Spectral Property, and Visual Information

Multiscale extension SSIM (MSSSIM) [23] is the extension of SSIM that focus on low-pass sub-sampling and filtering through variance and cross-correlation. The FLM approach was tested on MSSSIM with a score of less than 0.5, representing edge similarities in Table 3 images across the image scale. In some situations, for images with different spatial resolutions, the comparison is performed using Error Relative Global Dim Synthesis (ERGAS) [24]. ERGAS-based comparative approaches applied in Table 3 obtained results below 30 k. A close score of less than 20 k represents the similarity based on correlation and normalization. A Relative Average Square Error (RASE) [25] score ranging average to 3 k means good similarity among all the generated images. The Spectral Angle Mapper (SAM) evaluates the spectral angle formed between two image spectrums [26]. SAM treats image bands as vectors in spectral space. The angle with the lower value represents a closer match between the two image spectrums. In the table, our proposed approach secured a meager SAM value reflecting our model's efficiency. Visual Information Fidelity (VIFp) [27] achieves scores close to zero, representing close similarity among the model-generated and original images.

Table 3. MSSSIM, ERGAS, RASE, SAM, and VIFP evaluated on sample images.

Model Generated Image	Original Image	MSSSIM	ERGAS	RASE	SAM	VIFP
		(0.5021 + 0j)	16,381.1031	1573.8216	0.3577	0.0892
	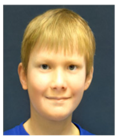	(0.3174 + 0j)	16,522.5801	2503.2524	0.3152	0.0823
	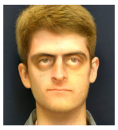	(0.3667 + 0j)	19,423.197	2807.7506	0.2728	0.0557
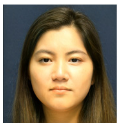		(0.3250 + 0j)	19,535.8021	2632.0759	0.3208	0.1354
	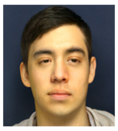	(0.3067 + 0j)	10,832.9807	2005.2324	0.3054	0.0720
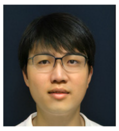		(0.3100 + 0j)	18,026.6801	2557.6952	0.3726	0.0990
		(0.2519 + 0j)	29,463.8512	4270.3793	0.5429	0.0299
		(0.5167 + 0j)	12,382.3081	1770.8513	0.3176	0.0993
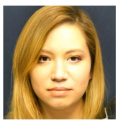		(0.2121 + 0j)	18,222.7227	2551.4187	0.2521	0.0382
		(0.2568 + 0j)	11,582.3176	2351.7226	0.3861	0.0392
		(0.2428 + 0j)	19,252.7421	2151.4684	0.2424	0.0186

Table 3. *Cont.*

Model Generated Image	Original Image	MSSSIM	ERGAS	RASE	SAM	VIFP
		(0.2167 + 0j)	11,583.2172	2551.7425	0.2863	0.0595
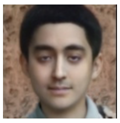		(0.4250 + 0j)	19,637.9001	2831.0789	0.4609	0.1253
		(0.4067 + 0j)	20,832.9807	3005.2324	0.4054	0.0720
		(0.5100 + 0j)	18,026.6801	2557.6952	0.3726	0.0990
		(0.3355 + 0j)	23,438.1978	3370.8904	0.4237	0.0716

6.3. Experiment carried out for the Level of Distortion Using Universal Quality Index

To observe the level of distortion in our generated output of the proposed approach, the Universal Image Quality Index (UIQI) [28] was evaluated on 100 selected images of the KinfaceW dataset. UIQI metric is a full reference image quality assessment technique to evaluate quality of an image by comparison. UIQI takes into account both enhance-ment and restoration for assessing the quality of image. The scores measured locally combined with the local region plotted in Figure 2. From Figure 2, it is observed that the loss of correlation and luminance distortion are in the proper balance within 0.2 to 0.5. Contrast distortions are also close but slightly more significant compared to other factors. For future work, this factor helps to set the hyper parameter to maintain all three aspects in equal measure, with the lower value representing a closer match between the two image spectrums. In the table, our proposed approach secured a meager SAM value reflecting our model's efficiency. Visual Information Fidelity (VIFp) [27] achieves scores close to zero, representing close similarity among the model-generated and original images.

6.4. Experiment for the Level of Distortion Using Universal Quality Index

FLM-generated images are very natural and difficult to distinguish as a machine generated output. To check the quality of the generated images, Blind/Reference less Image spatial Quality Evaluator (BRISQUE) [29] was applied on the results of the kinfaceW [30] dataset.

BRISQUE [29] first measures the distortion amount and prepares to extract natural scene statistics. Next, the pairwise neighborhood relationship using pixel intensities as a vector is established by subtracting the contrast normalization. In Figure 3, the red section represents the result evaluated on Kinface II, and the yellow bar represents Kinface I, two separate parts of the same dataset. Figure 3 shows that the proposed work achieves an excellent BRISQUE score for the Kinface I value ranging from 10 to 20. In Kinface II, the result varies depending on multiple images. Take this as the average.

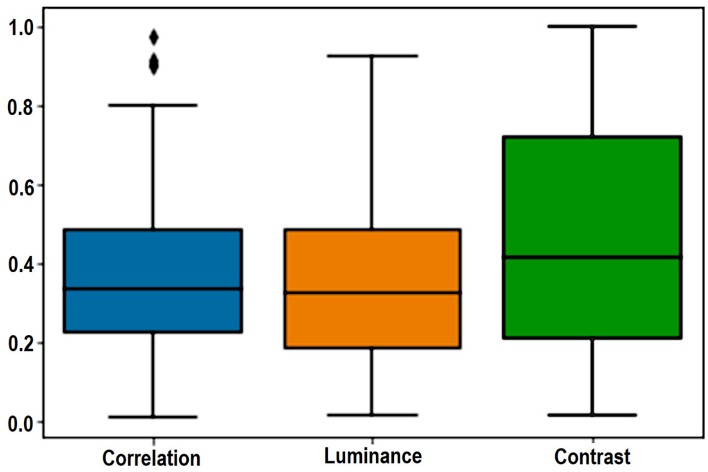

Figure 2. UQI evaluation score plot of kinfaceW dataset.

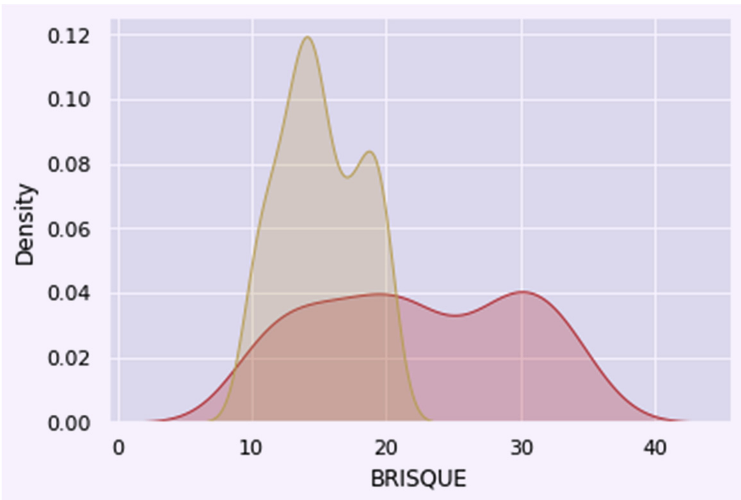

Figure 3. BRISQUE result on kinfaceW dataset generated result.

6.5. Experiment for Hyperparameter Selection

The proposed model tests 200 images of the KinfaceW [30] and Tufts [4] datasets. The dataset [30] contains unconstrained face images specially designed for kinship verification. The data are organized as a pair to determine the kin relationship between father, mother, daughter, and son.

The four biological relationships distribute within 134, 156, 127, and 116 pairs. Moreover, another part of the dataset [30] consists of 250 pairs of images. The KinfaceW [30] images are applied to the proposed approach to evaluate the future appearance of the children. The human observer assesses the generator-generated images. The Kin-faceW dataset designed to automatically determine kin or non-kin pairs through pre-serving facial expression based on genealogy records. This dataset provides valuable resource for biometric authentication, forensic investigations and genealogy research. The violin plot in Figure 4 represents the various hyperparameter evaluations based on the proposed method. Feature map one, learning rate two, and mapping net depth eight are F1L2M8. Based on this hyperparameter, the investigating officers generate the future appearance of the lost children based on the input such as in Figures 5–7.

6.6. Comparison Carried Out with Other Related Models

This section represents comparison between proposed work with other related state of the art models. Table 4 illustrates conceptual comparison along with limitations. Tables 5–8 contains detailed hyperparametric and architectural implementation details of other similar approaches compared with our FLM approach of Table 9.

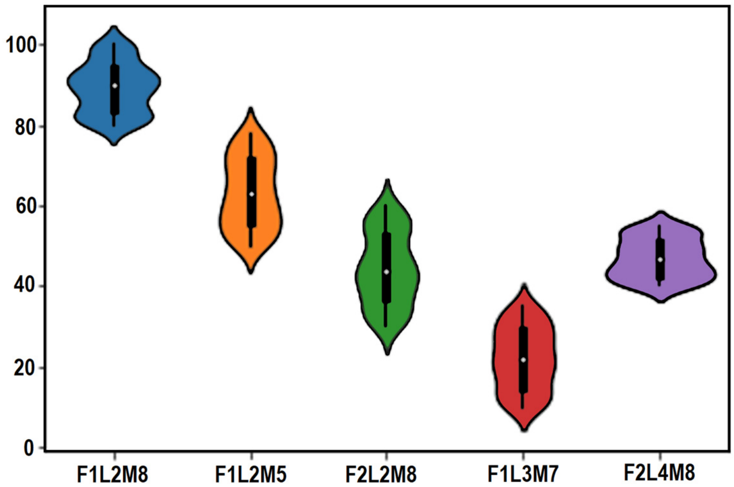

Figure 4. Human observer evaluation score on Multiple Hyperparameter.

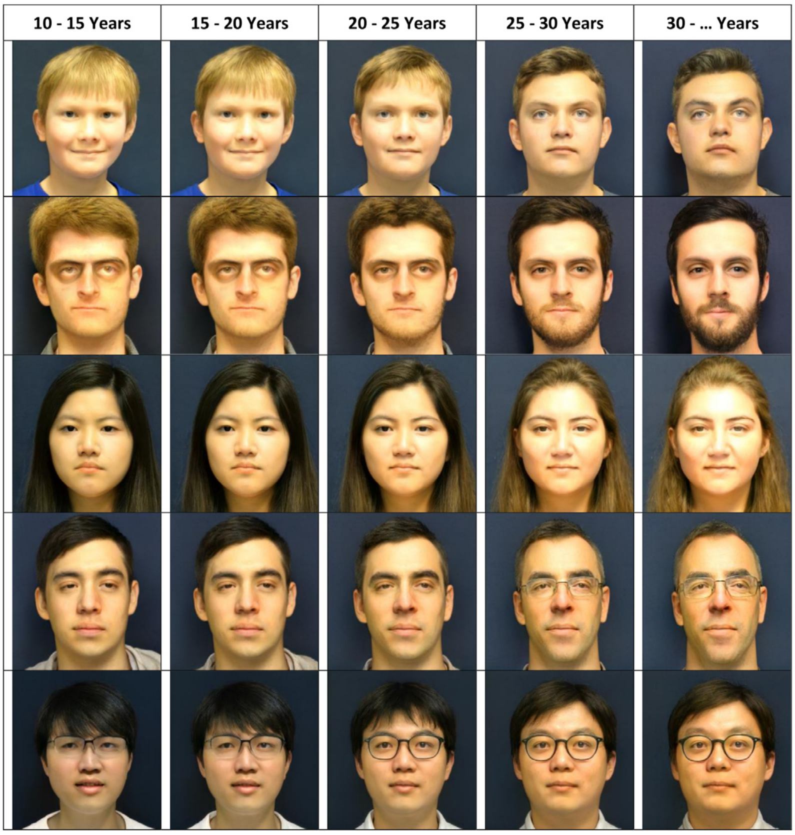

Figure 5. Model trained on F1L2M8 tested on Tufts face dataset sample set 1.

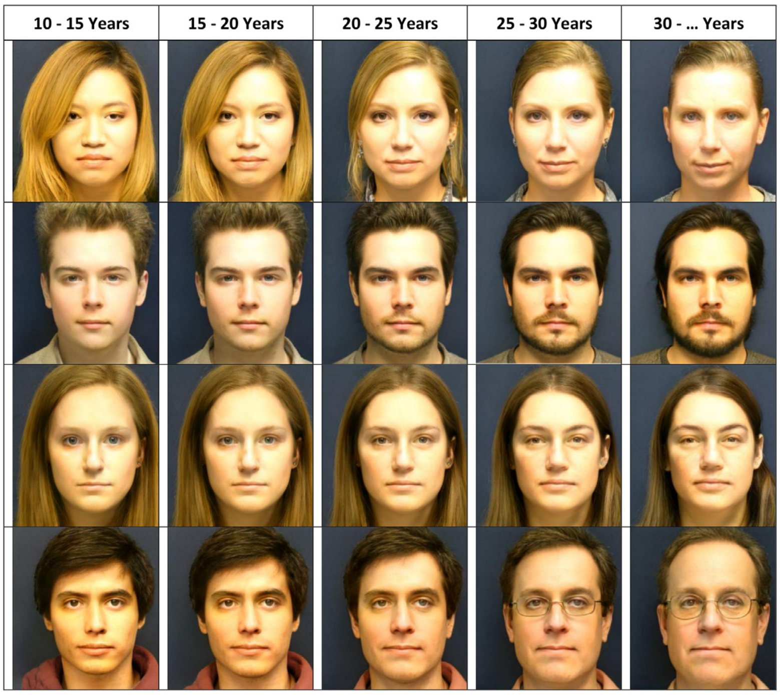

Figure 6. Model trained on F1L2M8 tested on Tufts face dataset sample set 2.

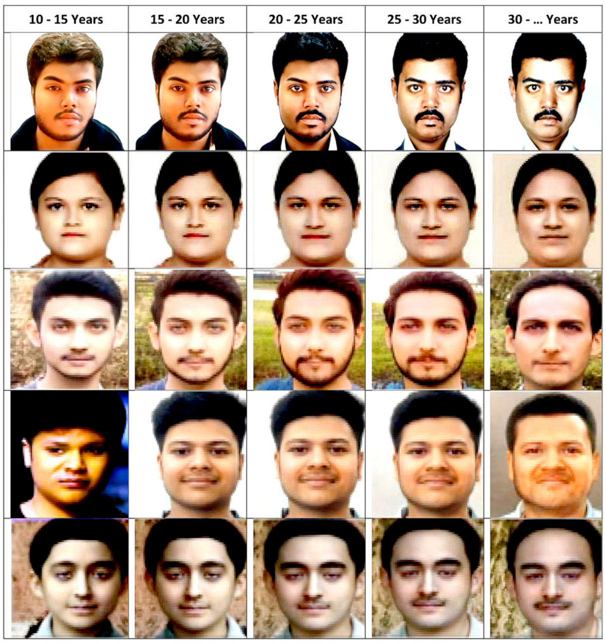

Figure 7. Model trained on F1L2M8 tested on selected real existing persons.

Table 4. Comparison of the proposed work with related models.

Model	Proposed Work	Limitation	Dataset
Latent Neural Fokker [9] –Planck kernels	It is a latent distribution-based approach with a plug and play implementation of GAN-based methods.	Dwinghyper-parameter tuning KL divergence became more sensitive.	CIFARIO [22]
MIPGAN [11]	The shelf verification and face recognition system [12] for studying vulnerability to generate new data.	Pre-selection of ethnicity, Mad performance detonated in empirical evaluation.	FFHQ [15]
AIRF [13]	This approach combines optimal morph field with Gaussian distribution to evaluate Bayes' formation.	The illustration is implemented, or the images are grayscale.	MIT face
AFR [14]	This method extracts facial landmark coordinates and averages them, splicing the visual flaws with inverse warping.	The local analysis of skin texture produces color inconsistencies.	ECVP [31], FET [32]
VAFM [33]	It is a combined approach based on OpenCV [34] and Face Morpher [33].	Lack of quality index factors.	FERET [35], FRGC [36], FRLL [37].
Our Model	It is based on StyleGan ADA with enhanced augmentation and scaling features.	Further research needs to be carried out for output quality improvement.	FFHQ [15], kinfaceW [30]

Table 5. Comparison of the proposed model with MIPGAN [11].

Model Generated Image	Original Image
MIPGAN [11]	
Network Architecture	Architecture of StyleGan [15]
Approach	The input latent code embedded into an intermediate latent space.
Convolutional Layer	3×3
Feature Maps	$1\times$
Weight Demodulation	StyleGan [15]
Path Length Regularization	X
Lazy Regularization	X
GPU	✓
Mixed Processor	X
Learning Rate	5
Optimizer	AMSGrad [38]

Table 6. Comparison with model [31] based on AMFIFV [15].

Model Generated Image	Original Image
	AMFIFV [13]
Network Architecture/Model	SPFM (Simple parameterized Face Model) [39]
Approach	Frontal view-based metamorphosis with automatic uniform illumination.
Convolutional Layer	–
Feature Maps	SPFM [39]
Weight Demodulation	Inverse Distance
Path Length Regularization	✓
Lazy Regularization	X
Number of GPU	–
Mixed Processor	X
Learning Rate	–

Table 7. Comparison with model [31] based on AFR [15].

Model Generated Image	Original Image
	AFR [16]
Network Architecture	Delaunay triangulations [40]
Approach	Forward and Backward Mapping performed to warp
Convolutional Layer	–
Feature Maps	[14]
Weight Demodulation	[14]
Path Length Regularization	X
Lazy Regularization	X
Number of GPU	–
Mixed Processor	X
Learning Rate	–

The architecture maintains style mixing by providing latent based inference evaluation. The order of magnitude amplifies features with style modulation. The learned affline transformation combines normalization with phase modulation during feature convolution. The architecture scales the convolution weight such that $\mathrm{w}_{\,c} = \mathrm{s}_k\mathrm{w}$, where w is the original weight and $\mathrm{w}_{\,c}$ represents the modulated weight. s_k represents the scale corresponding to k^{th} infant. Instant normalization updates output feature maps by eliminating the result of s_k from statistics. The standard deviation of the output activation is updated.

$$\sigma_i = \sqrt{\sum_{iK} w_{c_k} i^2} \tag{15}$$

Table 8. Comparison of the proposed model with VAFM [33].

Model Generated Image	**Original Image**
VAFM [33]	
Network Architecture Approach	FaceMorph [33], Webmorph [41]
Convolutional Layer	–
Feature Maps	–
Weight Demodulation	STASM [42]
Path Length Regularization	X
Lazy Regularization	X
Number of GPU	✓
Mixed Processor	X
Learning Rate	✓

Table 9. The Proposed Approach.

Model Generated Image	**Original Image**
Network Architecture	Revised architecture of AISG [1]
Approach	Broken into modulation based on feature map
Convolutional Layer	3×3
Feature Maps	$1\times$
Weight Demodulation	AISG [1]
Path Length Regularization	✓
Lazy Regularization	X
Number of GPU	1
Mixed Processor	X
Learning Rate	2
Mapping Net Depth	8

The demodulation is similar to the re-parameterized weight tensor. Formulate regularizations, $[I]_{m,n} \sim N(O,T)\left(\|K_S^P \chi\|_2 - b\right)^2$, where k_s represents the Jacobian matrix, X are random images, K_S^P represents explicit computation of the Jacobian matrix latent space point S, and the scale of the gradient is represented as b $\in \mathbb{R}$. AMFIFV [13] and uses Darwin's theory of natural evolution with (1+1)-ES algorithm [37] to prepare the initial population formulation on the face. Affline transformation acts as a mutation operator with scale and transformation parameters. The image deformation performed via warp generation requires feature mapping with source images. This approach leads to scattered data interpolation problems. The proposed approach uses augmentation with pixel blitting that does not require an inverse distance weighted interpolation method. AFR [14] uses Benford Features and a linear SVM classifier to perform training.

VAFM [33] is a software-based approach that uses the OpenCV landmark-based algorithm with WebMorph [41], an online tool and convolution layer for training [42–44]. FaceMorpher [33] is an open-source platform with a STASM [45] landmark detector. In Table 8, VAFM [33] is restricted to the FRLL dataset and is unable to obtain the expected result in another database such as FERET and FRGC [46]. The article also shows the calculations of MSE, RMSE, and PSNR [47,48]. Evaluation is performed on the parameters using 60 to 80 pixel cropping, an average of one scaling factor, and a minus three to three (degree) rotation angle. The AFR [14] approach in Table 9 lacks tampering detection. The AFR [14] also contains visual flaws while extracting the facial landmark.

7. Conclusions

The proposed approach obtains a BRISQE score within 10–30 by applying various flip and rotation mechanisms during pixel blitting. The score evaluated by comparing contrast, luminance and texture of the model generated pictorial statistics. Combining scaling and a few probabilistic transformations with StyleGan-ADA, the model obtains an SSIM score of 0.2 to 0.5 and MSSIM. For quality evaluation, the model brings a loss of correlation and luminance distortion within 0.2 to 0.5 during UQI [25] indexing. For future work, a few parameters need to change to balance the contrast distortion with loss of correlation and luminance distortion. To evaluate correlation and normalization, the proposed model scores 12 k to 23 k for ERGAS. The image spectrum was measured using SAM [26], score between, 0.2 to 0.5, reflecting its efficiency for generating output with reasonable accuracy. Such applications can also use for bioinformatics and other medical applications [49–51].

To carry out further research during pixel blitting, one can apply more color transformation strategies which improves the visual information fidelity (VIFP) score. During the experiment on hyperparameters, FLL2M5 scores quite near to the proposed FIL2M8.

Author Contributions: Conceptualization, methodology, and validation: B.B., B.D. and J.C.D.; formal analysis and investigation: B.B., S.K. and N.B.; resources and writing—review: B.B., B.D. and S.M.; writing—review and editing: S.M. and D.D. All authors have read and agreed to the published version of the manuscript.

Funding: This research received no external funding.

Data Availability Statement: The data is publicly available at http://tdface.ece.tufts.edu and https://www.kinfacew.com/datasets.html.

Acknowledgments: The authors would like to thank all the lab members of our institutes for their valuable suggestions, which improved the quality of the article.

Conflicts of Interest: The authors declare no conflict of interest.

Abbreviations

V	Convolution Kernel
$Z_\theta(e)$	Feature extraction function
e	Latent Feature
$\mathrm{C}\nu$	Cauchy Distribution
u	For any random variable
$\Phi_\mathrm{u}(\nu)$	Generating Function
$U_1, U_2, \ldots, U_N$	Independent random variable distributed with fixed latent
$R_1, R_2, \ldots, R_N$	Set of deterministic projection
O_i	Identity Operator
${t_n}^r$ and ${t_m}^g$	Unique Distribution
$\mathrm{t_a}, \mathrm{t_b}$	Transformation Variable
Θ	Rotation Angle
$(\mathrm{P_0}, \mathrm{P_{ni}})$	Variable for padding
$\mathcal{U}(.)$	Uniform Distribution
M	Pixel value accumulated into matrix for image
T	Translation Matrix

References

1. Karras, T.; Aittala, M.; Hellsten, J.; Laine, S.; Lehtinen, J.; Aila, T. Training generative adversarial networks with limited data. *Adv. Neural Inf. Process. Syst.* **2020**, *33*, 12104–12114.
2. Kennett, D. Using genetic genealogy databases in missing persons cases and to develop suspect leads in violent crimes. *Forensic Sci. Int.* **2019**, *301*, 107–117. [CrossRef] [PubMed]
3. Tong, C.; Li, Y.; Jacob, A.P.; Bengio, Y.; Li, W. Mode regularized generative adversarial networks. *arXiv* **2016**, arXiv:1612.02136.

4. Karen, P.; Wan, Q.; Agaian, S.; Rajeev, S.; Kamath, S.; Rajendran, R.; Rao, S.; Rao, S.P.; Kaszowska, A.; Taylor, H.; et al. A comprehensive database for benchmarking imaging systems. *IEEE Trans. Pattern Anal. Mach. Intell.* **2018**, *42*, 509–520.
5. Teterwak, P.; Sarna, A.; Krishnan, D.; Maschinot, A.; Belanger, D.; Liu, C.; Freeman, W.T. Boundless: Generative adversarial networks for image extension. In Proceedings of the IEEE/CVF International Conference on Computer Vision, San Francisco, CA, USA, 19 June 1985; pp. 10521–10530.
6. Cai, Z.; Xiong, Z.; Xu, H.; Wang, P.; Li, W.; Pan, Y. Generative adversarial networks: A survey toward private and secure applications. *ACM Comput. Surv. (CSUR)* **2021**, *54*, 1–38. [CrossRef]
7. Jabbar, A.; Li, X.; Omar, B. A survey on generative adversarial networks: Variants, applications, and training. *ACM Comput. Surv. (CSUR)* **2021**, *54*, 1–49. [CrossRef]
8. Pascual, S.; Bonafonte, A.; Serra, J. SEGAN: Speech enhancement generative adversarial network. *arXiv* **2017**, arXiv:1703.09452.
9. Yufan, Z.; Chen, C.; Xu, J. Learning High-Dimensional Distributions with Latent Neural Fokker-Planck Kernels. *arXiv* **2021**, arXiv:2105.04538.
10. Goodfellow, I.; Pouget-Abadie, J.; Mirza, M.; Xu, B.; Warde-Farley, D.; Ozair, S.; Courville, A.; Bengio, Y. Generative adversarial networks. *Commun. ACM* **2020**, *63*, 139–144. [CrossRef]
11. Zhang, H.; Venkatesh, S.; Ramachandra, R.; Raja, K.; Damer, N.; Busch, C. MIPGAN-Generating Strong and High Quality Morphing Attacks Using Identity Prior Driven GAN. *IEEE Trans. Biom. Behav. Identity Sci.* **2021**, *3*, 365–383. [CrossRef]
12. Schaefer, S.; McPhail, T.; Warren, J. Image deformation using moving least squares. In *ACM SIGGRAPH 2006 Papers*; Association for Computing Machinery: New York, NY, USA, 2006; pp. 533–540.
13. Bichsel, M. Automatic interpolation and recognition of face images by morphing. In Proceedings of the Second International Conference on Automatic Face and Gesture Recognition, Killington, Vermont, 14–16 October 1996; IEEE: New York, NY, USA, 1996.
14. Makrushin, A.; Neubert, T.; Dittmann, J. Automatic generation and detection of visually faultless facial morphs. In Proceedings of the International Conference on Computer Vision Theory and Applications, Porto, Portugal, 27 February–1 March 2017; SciTePress: Setubal, Portugal, 2017.
15. Tero, K.; Laine, S.; Aila, T. A style-based generator architecture for generative adversarial networks. In Proceedings of the IEEE/CVF Conference on Computer Vision and Pattern Recognition, Long Beach, CA, USA, 15–20 June 2019; pp. 4401–4410.
16. DeVries, T.; Taylor, G.W. Improved regularization of convolutional neural networks with cutout. *arXiv* **2017**, arXiv:1708.04552.
17. Anwar, S.; Meghana, S. A pixel permutation based image encryption technique using chaotic map. *Multimed. Tools Appl.* **2019**, *78*, 27569–27590. [CrossRef]
18. Atkins, C.B.; Bouman, C.A.; Allebach, J.P. Optimal image scaling using pixel classification. In Proceedings of the 2001 International Conference on Image Processing (Cat. No. 01CH37205), Thessaloniki, Greece, 7–10 October 2001; IEEE: New York, NY, USA, 2001.
19. Jamitzky, F.; Stark, R.W.; Bunk, W.; Thalhammer, S.; Räth, C.; Aschenbrenner, T.; Morfill, G.E.; Heckl, W.M. Scaling-index method as an image processing tool in scanning-probe microscopy. *Ultramicroscopy* **2001**, *86*, 241–246. [CrossRef] [PubMed]
20. Prashanth, H.S.; Shashidhara, H.L.; Murthy, K.B. Image scaling comparison using universal image quality index. In Proceedings of the 2009 International Conference on Advances in Computing, Control, and Telecommunication Technologies, Bangalore, India, 28–29 December 2009; IEEE: New York, NY, USA, 2009.
21. Bora, A.; Price, E.; Dimakis, A.G. *AmbientGAN: Generative Models from Lossy Measurements, Vancouver Convention Center, Vancouver, BC, Canada, 30 April–3 May 2018*; ICLR, 2018.
22. The CIFAR-10 Dataset. Available online: https://www.cs.toronto.edu/~kriz/cifar.html (accessed on 2 February 2023).
23. Rouse, D.M.; Hemami, S.S. Understanding and simplifying the structural similarity metric. In Proceedings of the 15th International Conference on Image Processing, Vietri sul Mare, Italy, 12 October 2008; IEEE: New York, NY, USA, 2008; pp. 1188–1191.
24. Renza, D.; Martinez, E.; Arquero, A. A new approach to change detection in multispectral images by means of ERGAS index. *IEEE Geosci. Remote Sens. Lett.* **2012**, *10*, 76–80.
25. Willmott, C.J.; Matsuura, K. Advantages of the mean absolute error (MAE) over the root mean square error (RMSE) in assessing average model performance. *Clim. Res.* **2005**, *30*, 79–82.
26. Yang, C.; Everitt, J.H.; Bradford, J.M. Yield estimation from hyperspectral imagery using spectral angle mapper (SAM). *Trans. ASABE* **2008**, *51*, 729–737. [CrossRef]
27. Kuo, T.Y.; Su, P.C.; Tsai, C.M. Improved visual information fidelity based on sensitivity characteristics of digital images. *J. Vis. Commun. Image Represent.* **2016**, *40*, 76–84. [CrossRef]
28. Wang, Z.; Bovik, A.C. A universal image quality index. *IEEE Signal Process. Lett.* **2002**, *9*, 81–84. [CrossRef]
29. Mittal, A.; Moorthy, A.K.; Bovik, A.C. Blind/referenceless image spatial quality evaluator. In Proceedings of the Conference Record of the Forty Fifth Asilomar Conference on Signals, Systems and Computers (ASILOMAR), Pacific Grove, CA, USA, 6–9 November 2011; IEEE: New York, NY, USA, 2011; pp. 723–727.
30. Lu, J.; Zhou, X.; Tan, Y.P.; Shang, Y.; Zhou, J. Neighborhood repulsed metric learning for kinship verification. *IEEE Trans. Pattern Anal. Mach. Intell.* **2014**, *7*, 331–345.
31. Psychological Image Collection at Stirling (PICS). Available online: http://pics.psych.stir.ac.uk/2D_face_sets.htm (accessed on 12 January 2023).
32. FEI Face Database. Available online: http://fei.edu.br/~cet/facedatabase.htm (accessed on 8 February 2023).
33. Eklavya, S.; Korshunov, P.; Colbois, L.; Marcel, S. Vulnerability analysis of face morphing attacks from landmarks and generative adversarial networks. *arXiv* **2020**, arXiv:2012.05344.

34. Khan, M.; Chakraborty, S.; Astya, R.; Khepra, S. Face detection and recognition using OpenCV. In Proceedings of the 2019 International Conference on Computing, Communication, and Intelligent Systems (ICCCIS), Greater Noida, India, 18–19 October 2019; pp. 116–119.
35. Phillips, P.J.; Wechsler, H.; Huang, J.; Rauss, P.J. The FERET database and evaluation procedure for face-recognition algorithms. *Image Vis. Comput.* **1998**, *4*, 295–306.
36. Phillips, P.J.; Flynn, P.J.; Scruggs, T.; Bowyer, K.W.; Chang, J.; Hoffman, K.; Marques, J.; Min, J.; Worek, W. Overview of the face recognition grand challenge. In Proceedings of the 2005 IEEE Computer Society Conference on Computer Vision and Pattern Recognition (CVPR'05), San Diego, CA, USA, 20–25 June 2005; IEEE: New York, NY, USA, 2005; Volume 1, pp. 947–954.
37. Kozyra, K.; Trzyniec, K.; Popardowski, E.; Stachurska, M. Application for Recognizing Sign Language Gestures Based on an Artificial Neural Network. *Sensors* **2022**, *22*, 9864. [CrossRef] [PubMed]
38. Back, T.; Gunter, R.; Hans-Paul, S. Evolutionary Programming and Evolution Strategies: Similarities and Differences. In Proceedings of the Second Annual Conference on Evolutionary Programming, Evolutionary Programming Society, San Francisco, CA, USA, 10–12 July 1993; pp. 11–22.
39. Salimans, T.; Goodfellow, I.; Zaremba, W.; Cheung, V.; Radford, A.; Chen, X. Improved techniques for training GANs. In Proceedings of the 30th Conference on Neural Information Processing System (NIPS), Bercelona, Spain, 5–10 December 2016.
40. Federic, P.; Keith, W. *Computer Facial Animation*; AK Peters: Wellesley, MA, USA, 1996.
41. *Lecture Notes Series on Computing: Volume 4, Computing in Euclidean Geometry*, 2nd ed.; World Scientific: Singapore, 1995; pp. 225–265. Available online: https://www.worldscientific.com/worldscibooks/10.1142/2463#t=aboutBook (accessed on 11 December 2022).
42. Das, H.S.; Das, A.; Neog, A.; Mallik, S.; Bora, K.; Zhao, Z. Early detection of Parkinson's disease using fusion of discrete wavelet transformation and histograms of oriented gradients. *Mathematics* **2022**, *10*, 4218. [CrossRef]
43. Ghosh, S.; Banerjee, S.; Das, S.; Hazra, A.; Mallik, S.; Zhao, Z.; Mukherji, A. Evaluation and Optimization of Biomedical Image-Based Deep Convolutional Neural Network Model for COVID-19 Status Classification. *Appl. Sci.* **2022**, *12*, 10787. [CrossRef]
44. Bhandari, M.; Neupane, A.; Mallik, S.; Gaur, L.; Qin, H. Auguring Fake Face Images Using Dual Input Convolution Neural Network. *J. Imaging* **2022**, *9*, 3. [CrossRef] [PubMed]
45. Liu, C.; Chen, K.; Xu, Y. Study of face recognition technology based on STASM and its application in video retrieval. In *Computational Intelligence, Networked Systems and Their Applications: International Conference of Life System Modeling and Simulation, LSMS 2014 and International Conference on Intelligent Computing for Sustainable Energy and Environment, ICSEE 2014, Shanghai, China, 20–23 September 2014, Proceedings, Part II*; Springer: Berlin/Heidelberg, Germany, 2014; pp. 219–227.
46. Milborrow, S.; Nicolls, F. *Active Shape Models with SIFT Descriptors and MARS*; VISAPP: Setubal, Portugal, 2014.
47. Saladi, S.; Karuna, Y.; Koppu, S.; Reddy, G.R.; Mohan, S.; Mallik, S.; Qin, H. Segmentation and Analysis Emphasizing Neonatal MRI Brain Images Using Machine Learning Techniques. *Mathematics* **2023**, *11*, 285. [CrossRef]
48. Bora, K.; Mahanta, L.B.; Borah, K.; Chyrmang, G.; Barua, B.; Mallik, S.; Zhao, Z. Machine Learning Based Approach for Automated Cervical Dysplasia Detection Using Multi-Resolution Transform Domain Features. *Mathematics* **2022**, *10*, 4126. [CrossRef]
49. Levi, O.; Mallik, M.; Arava, Y.S. ThrRS-Mediated Translation Regulation of the RNA Polymerase III Subunit RPC10 Occurs through an Element with Similarity to Cognate tRNA ASL and Affects tRNA Levels. *Genes* **2023**, *14*, 462. [CrossRef]
50. Mallik, S.; Seth, S.; Bhadra, T.; Zhao, Z. A Linear Regression and Deep Learning Approach for Detecting Reliable Genetic Alterations in Cancer Using DNA Methylation and Gene Expression Data. *Genes* **2020**, *11*, 931. [CrossRef]
51. Mallik, S.; Mukhopadhyay, A.; Maulik, U. RANWAR: rank-based weighted association rule mining from gene expression and methylation data. *IEEE Trans. Nanobioscience* **2014**, *14*, 59–66.